Assessment of natural gas hydrate reservoirs at Site GMGS3–W19 in the Shenhu area, South China Sea based on various well logs

Dong–ju Kang, Ying–feng Xie, Jing–an Lu, Tong Wang, Jin–qiang Liang, Hong–fei Lai, Yun–xin Fang

Citation: Dong–ju Kang, Ying–feng Xie, Jing–an Lu, Tong Wang, Jin–qiang Liang, Hong–fei Lai, Yun–xin Fang, 2022. Assessment of natural gas hydrate reservoirs at Site GMGS3–W19 in the Shenhu area, South China Sea based on various well logs, China Geology, 5, 383–392. doi: 10.31035/cg2022025.

View online: https://doi.org/10.31035/cg2022025

China Geology 5 (2022) 383−392

China Geology

Journal homepage: http://chinageology.cgs.cn
https://www.sciencedirect.com/journal/china-geology

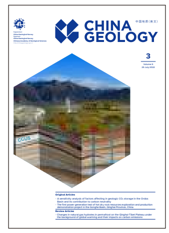

Assessment of natural gas hydrate reservoirs at Site GMGS3-W19 in the Shenhu area, South China Sea based on various well logs

Dong-ju Kang[a, b], Ying-feng Xie[a, b,*], Jing-an Lu[a, b], Tong Wang[a, b], Jin-qiang Liang[a, b], Hong-fei Lai[a, b], Yun-xin Fang[a, b]

[a] Southern Marine Science and Engineering Guangdong Laboratory (Guangzhou), Guangzhou 511458, China
[b] Guangzhou Marine Geological Survey, China Geological Survey, Ministry of Natural Resources, Guangzhou 510075, China

ARTICLE INFO

Article history:
Received 19 July 2021
Received in revised form 2 March 2022
Accepted 1 April 2022
Available online 25 April 2022

Keywords:
Natural gas hydrates (NGHs)
Low gamma
Reservoir properties
Saturation
NMR
Marine hydrates trial exploration engineering
Shenhu area
South China Sea

ABSTRACT

To obtain the characteristics of the gas hydrate reservoirs at GMGS3-W19, extensive geophysical logging data and cores were analyzed to assess the reservoir properties. Sediment porosities were estimated from density, neutron, and nuclear magnetic resonance (NMR) logs. Both the resistivity and NMR logs were used to calculate gas hydrate saturations, the Simandoux model was employed to eliminate the effects of high clay content determined based on the ECS and core data. The density porosity was closely in agreement with the core-derived porosity, and the neutron porosity was higher while the NMR porosity was lower than the density porosity of sediments without hydrates. The resistivity log has higher vertical resolution than the NMR log and thus is more favorable for assessing gas hydrate saturation with strong heterogeneity. For the gas hydrate reservoirs at GMGS3-W19, the porosity, gas hydrate saturation and free gas saturation was 52.7%, 42.7% and 10%, on average, respectively. The various logs provide different methods for the comprehensive evaluation of hydrate reservoir, which supports the selection of candidate site for gas hydrate production testing.

1. Introduction

Natural gas hydrates (NGHs) are crystalline solids that contain gas molecules encaged in water molecules. Gas hydrate reservoirs are considered to contain abundant cleaner energy than other conventional hydrocarbon sources. Several production tests have shown significant progress in the understanding that natural gas can be produced from reservoirs by using advanced production technologies (Yamamoto K et al., 2014; Li JF et al., 2018; Cui Y et al., 2018; Ye JL et al., 2020).

The Guangzhou Marine Geological Survey (GMGS) implemented gas hydrate drilling expeditions in 2007 and 2013 in the South China Sea. Gas hydrates were recovered from Fugro pressure cores during the expeditions, confirming the presence of gas hydrates in the South China Sea (Zhang GX et al., 2007; Zhang HQ et al., 2014). In 2015, with improved recognition and increased knowledge obtained from newly acquired geophysical and geochemical data, the GMGS3 was conducted in the Shenhu area. Comprehensive well logs obtained in the area were used to accurately assess the gas hydrate reservoir properties and to assist in selecting ideal candidate sites for potential gas hydrate production testing in the future. It is well known that the development effectiveness of these gas hydrate reservoirs relies heavily on key reservoir parameters, including porosity, gas hydrate saturation, gas saturation, and reservoir thickness. Therefore, it is important to understand these critical parameters before developing a drilling plan for a gas hydrate production test (Li Y et al., 2021). This study aims to assess the reservoir properties at GMGS3-W19, a candidate site selected for potential gas hydrate production testing due to its high concentration and porosity. To this end, this study first introduces the identification of gas hydrate and free gas intervals based on various logs coupled with core data. Then, it focuses on the characterization of the gas hydrate reservoirs including accurate mineral components, porosity, and gas

First author: *E-mail address*: dongjukang@163.com (Dong-ju Kang).

* Corresponding author: *E-mail address*: xieyingfeng_gmgs@163.com (Ying-feng Xie).

Literary editor: Xi-jie Chen
doi:10.31035/cg2022025
2096-5192/

hydrate/gas saturations based on various well logs and core data.

2. Natural gas hydrates occurrence

Five logging while drilling (LWD) tools provided by Schlumberger were deployed at Site W19, namely geoVISION (felectrical imaging), SonicScope675 (multipole acoustic logging), NeoScope (density and neutron porosity), proVISION (NMR porosity), and Telescope (MWD). General well-log data such as gamma, density, and neutron porosity logs and deep resistivity logs based on acoustic travel time, along with various investigation depths of resistivity images and NMR were used in this study. Fig. 1 shows the characteristic log response of the entire hole at the site of W19.

The resistivity and velocity logs can be used to identify and assess gas hydrates (Collett TS and Ladd J, 2000; Lee MW and Collett TS, 2009, 2011, 2012; Shankar U and Riedel M, 2014). As shown in Fig. 1, the top of the gas hydrate zone was determined at a depth of 135 mbsf based on the abruptly increasing resistivity, lower acoustic travel time, and high brightness on the resistivity images. It was inferred that base of the gas hydrate zone was at a depth of 162 mbsf from the following observations: (1) The Fugro Marine Core Barrel (FMCB) coring at the interval (160.5–163.5 mbsf) of adjacent coring well W19B showed low-temperature anomalies at the top of the core but warmness in the bottom; (2) The base depth of the gas hydrate stability zone was calculated to be about 162 mbsf according to *in situ* temperature measurements (the seafloor temperature and geothermal gradient are 4° and 56.1°/km, respectively); (3) The density and neutron porosity logs show an abrupt decrease in value at the depth of 162 mbsf. It is noteworthy that the density and neutron porosity logs are also inversely crossed. In addition, the sonic slowness-time coherence becomes weak within the gas hydrate interval between 144.6 mbsf and 157 mbsf, which is believed to be caused by free gas. The gas may originate from the gas hydrate dissociation in the drilling process or originally coexist with gas hydrates, as discussed below. The higher resistivity (compared to the baseline of the formation resistivity) and lower density, neutron porosity, and velocities suggest the presence of free gas at a depth of approximately 162–190 mbsf.

As shown in Fig. 1, the T2 spectrum is discontinuous due to the measurement failure of the proVISION tool in some sections. Fortunately, some valuable NMR log data were acquired in the upper part of the gas hydrate zone. Since the measurements of NMR and density porosity are not dependent on the interactions between the gas hydrates and porous media (Bauer K et al., 2015; Lee MW and Collet TS, 2011), the authors attempt to assess the gas hydrate saturation using the limited, discontinuous NMR data.

3. Mineral composition calculation

The integration of X-ray diffraction (XRD) and LWD techniques is commonly used to provide information on mineral composition, mineral types, and their content for reservoir characterization (Kang DJ et al., 2018; Wei JG et al., 2018). According to X-ray diffraction analyses of core samples, the W19 reservoir is primarily composed of quartz, calcite, and clay, and trace quantities of plagioclase, dolomite, pyrite, augite, and anhydrite (Table 1). Among them, quartz, calcite, and clay are the most abundant minerals, with an average content of 25.4%, 27.2% and 27.2%, respectively. Meanwhile, the clay has a content of 11.5% –46.9% and mainly includes illite (27%–53%, average: 39.4%) and illite/montmorillonite (22%–50%, average: 38.9%).

The XRD results were input as calibration points to

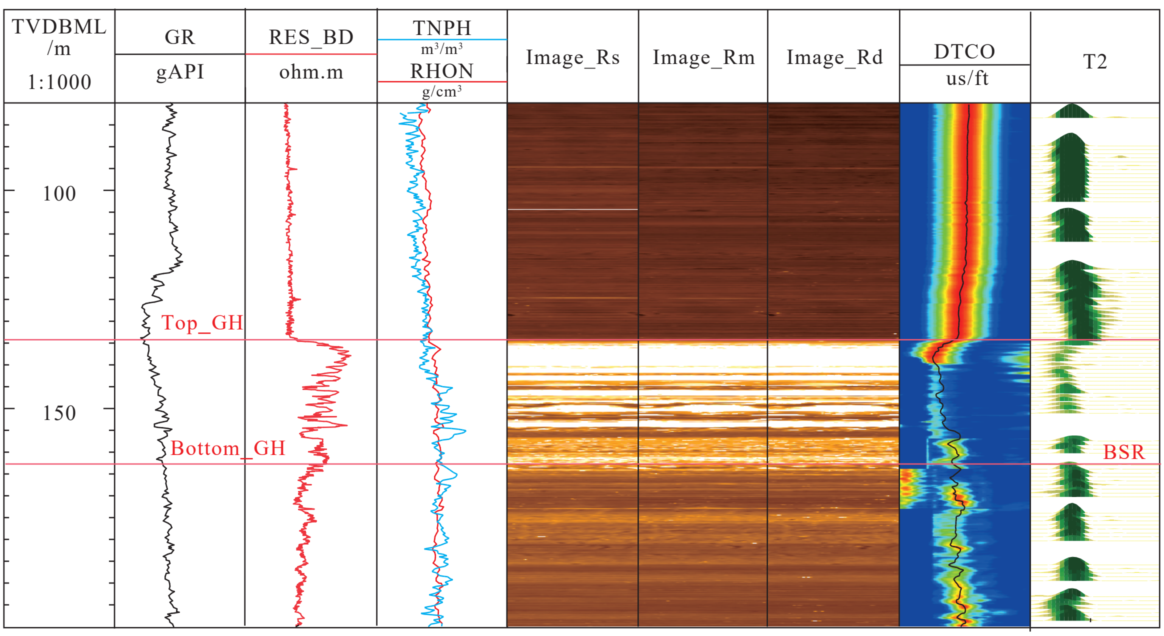

Fig. 1. Downhole LWD results at the site of Well W19.

Table 1. Content of sediment components obtained from X-ray diffraction analyses of Site W19.

Mineral component	Average content/%
Quartz	25.4
Plagioclase	6.2
Calcite	27.2
Dolomite	4.8
Pyrite	2.44
Anhydrite	3.53
Augite	3.68
Clay	27.2

calculate the continuous mineral composition from ECS logs coupled with the other conventional logs, and the calculated mineral composition is shown in Fig. 2. In this figure, the first column is the true vertical depth below mudline (TVDBML), the second column is the gamma ray log, the third column is the resistivity log, the fourth to eighth columns are the weight percentages of Al, Ca, Fe, Si and S, respectively, and the ninth to eleventh columns show the comparison of the calculated content of quartz + plagioclase, carbonate (calcite + dolomite), clay, and pyrite with the XRD data. According to the Fig. 2, the calculated mineral composition agreed well with the core data, especially within the interval between 119 mbsf and 146 mbsf, which consists of a 16 m thick non-hydrate reservoir and a 10 m thick upper hydrate reservoir. The gamma values were notably low within the interval between 119 mbsf and 146 mbsf, which is often associated with sands. However, the weight of calcareous materials notably increased according to the processing result of ECS logs, which is also consistent with the core data because although the quartz content of the low gamma ray zone did not significantly increase, the average carbonate content increased from 25% in the upper zone to 43% in the low gamma zone according to the XRD results. Based on these and the thin section identification results, it can be confirmed that the low gamma ray activity zone is caused by the high content of calcareous materials with abundant sand-sized foraminifera, which are also visible near Site W18 (Kang DJ et al., 2018).

4. Porosity calculations

Sediment porosities can be determined according to various borehole logging measurements (Fujii T et al., 2015). This study used the data from the density, neutron porosity, and NMR logs to calculate sediment porosities at Site W19.

The equation commonly used to calculate porosity from

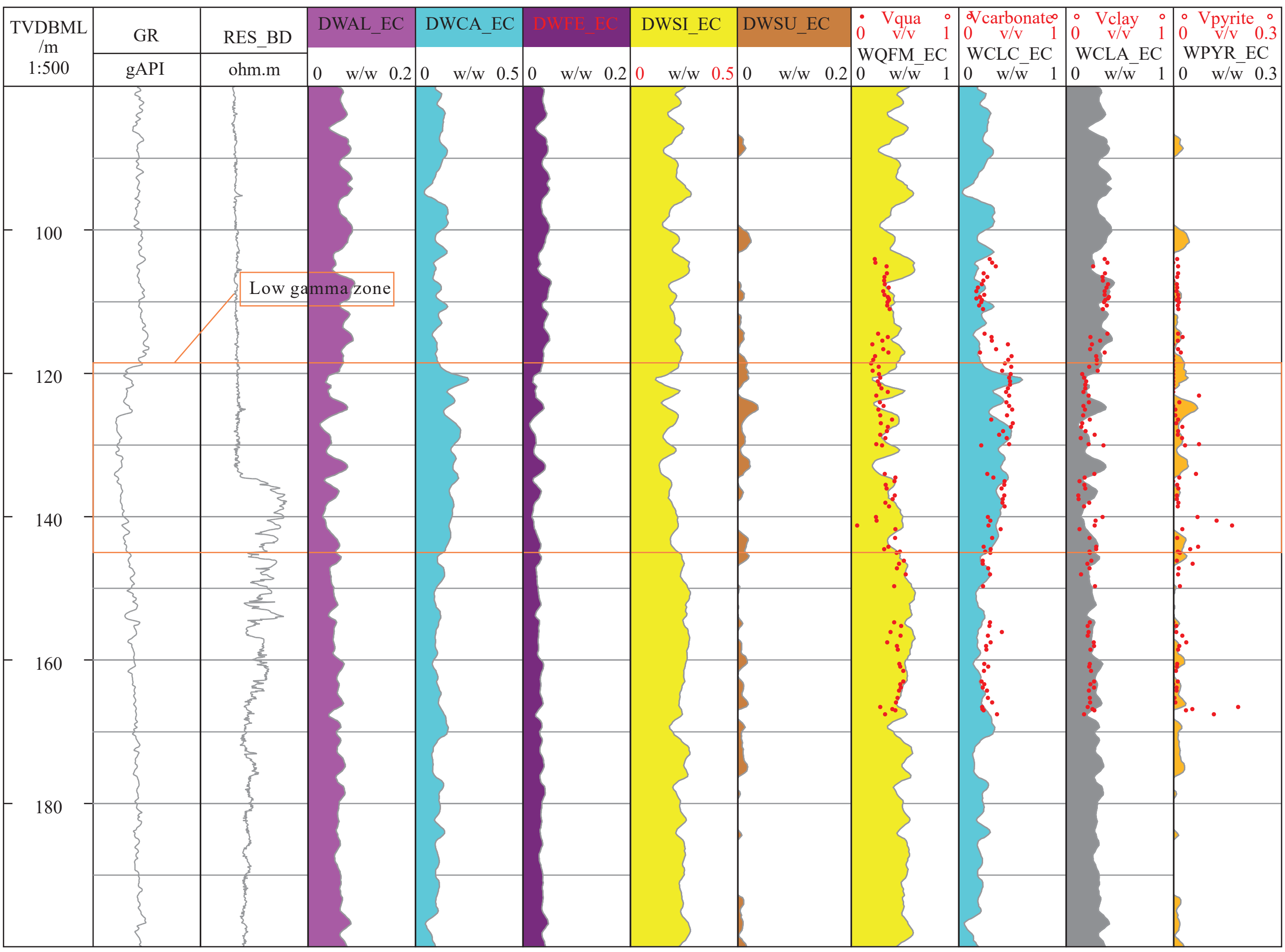

Fig. 2. Comparison of the mineral component results with ECS processing and laboratory analysis at Site W19.

density logging is as follows:

$$\varphi_{d-ecs} = \frac{\rho_{m-ecs} - \rho_b}{\rho_{m-ecs} - \rho_f} \tag{1}$$

where φ_{d-ecs} is the porosity based on an ECS-derived matrix density, ρ_f is the fluid density, which is assumed to be $\rho_f = 1.04$ g/cm^3, and ρ_b is the measured formation density. ρ_{m-ecs} is the matrix density, which varies with mineral composition and corresponding content. Since each mineral has a specific density value as shown in Table 2, ρ_{m-ecs} is calculated using the following equation to obtain accurate porosity:

$$\rho_{m-ecs} = \sum V_i \rho_i \tag{2}$$

where V_i represents the volume content of each mineral, and ρ_i is the density of each mineral.

According to the mineral composition obtained through the processing of the ECS log, anhydrite exists in the entire hole at Site W19 aside from dominant components such as quartz, calcite, and clay. The core data show that the anhydrite has an average content of 3.5%, which cannot be determined according to the ECS logging data. The anhydrite mineral was also used as input to calculate the matrix density.

Core porosity represents the total water content of the sediments including interlayer, bound, and free water (Collett TS and Ladd J, 2000; Suzuki K et al., 2015). The density log also measures the total water content of the sediments, and thus the density porosity of sediments should be roughly equal to the core porosity (Collett TS and Ladd J, 2000) The calculated grain density and porosity determined using equations (1) and (2) are shown in Fig. 3. It shows that the calculated results of grain density and porosity are consistent with the core-derived grain density and porosity. Moreover, the enlarged borehole part from the seafloor to the depth of 20 mbsf had a significant effect on the values of the calculated grain density and porosity. Below the depth of 20 mbsf, the grain density ranged from a maximum of about 2.77 g/cm^3 to a minimum value of about 2.67 g/cm^3, with an average of 2.72 g/cm^3 and the porosity calculation yielded values ranging from about 45% to 68%, with an average of 52.7% at Site W19.

For Site W19, aside from the density porosity, the sediment porosity was also calculated from the thermal neutron and limited nuclear magnetic logs, as shown in Fig. 4. According to Fig. 4a, the thermal neutron porosity was higher while the NMR porosity was lower than the density log-derived porosities above the gas hydrate zone. Neutron log measured the total amount of hydrogen in the formation, and the presence of crystal water within clay minerals was the primary reason for the elevated the neutron porosity. The neutron porosity decreases when free gas occurs in the pore space due to the low hydrogen index in the gas. The NMR measurement is aimed at obtaining information on hydrogen nuclei in pore fluid, so it can effectively reflect the total porosity of reservoirs while avoiding the influence of lithology (Kenyon WE, 1992; Latour LL et al., 1995). However, the NMR log is liable to be affected by many factors, such as echo string acquisition parameters, the signal-to-noise ratio of echo string, and the salinity of drilling fluid (Kleinberg RL, 1999; Kleinberg RL et al., 2003). It is considered that the low NMR porosity at Site W19 was induced by the long echo interval (0.8 ms) of the proVISION tool. The shorter the echo interval of a NMR logging tool, the higher the accuracy of measured clay-bound water (Zhong J et al., 2019). Owing to the large echo interval, information on some small pores filled with clay-bound water at Site W19 was lost, resulting in the lower NMR porosity compared to the density porosity. A quick approach can be applied to the correction of porosities calculated from the neutron and NMR logs. The neutron porosity and the NMR porosity were corrected by reducing by a factor of 0.09 and increasing by a factor of 0.16, respectively to make them agree well with the density porosity at a depth of about 10–135 mbsf at Site W19 (Figs. 4b, 4c). The discrepancy between the corrected neutron porosity and density porosity occurred at a depth of 120–190 mbsf, which was mainly induced by free gas. Meanwhile, the gas hydrates in the formation contributed to the discrepancy

Table 2. Density of different mineral components.

Mineral	Quartz	Calcite	Illite	Pyrite	Anhydrite
Density/(g/cm^3)	2.65	2.73	2.42	4.99	2.98

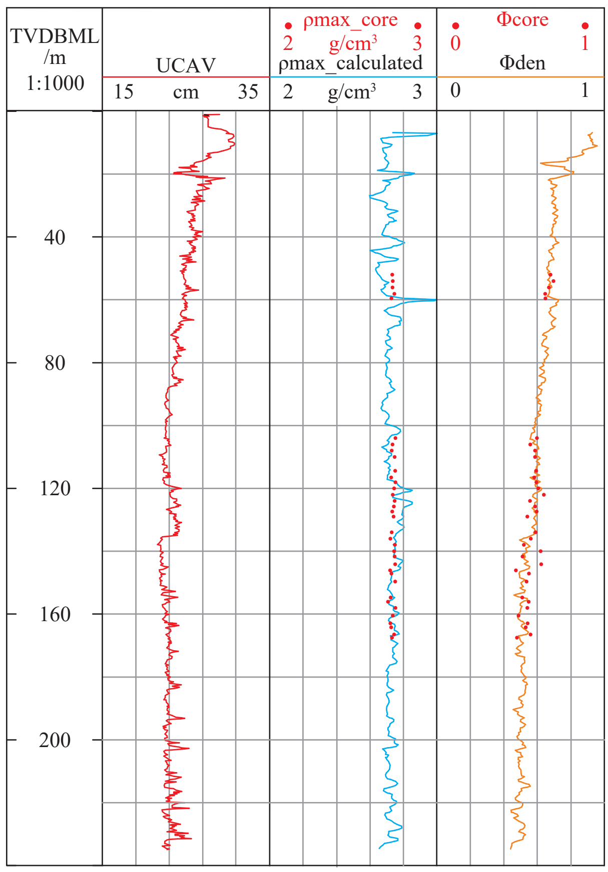

Fig. 3. Comparison of calculated grain density and density porosity using the ECS log with core analytical results.

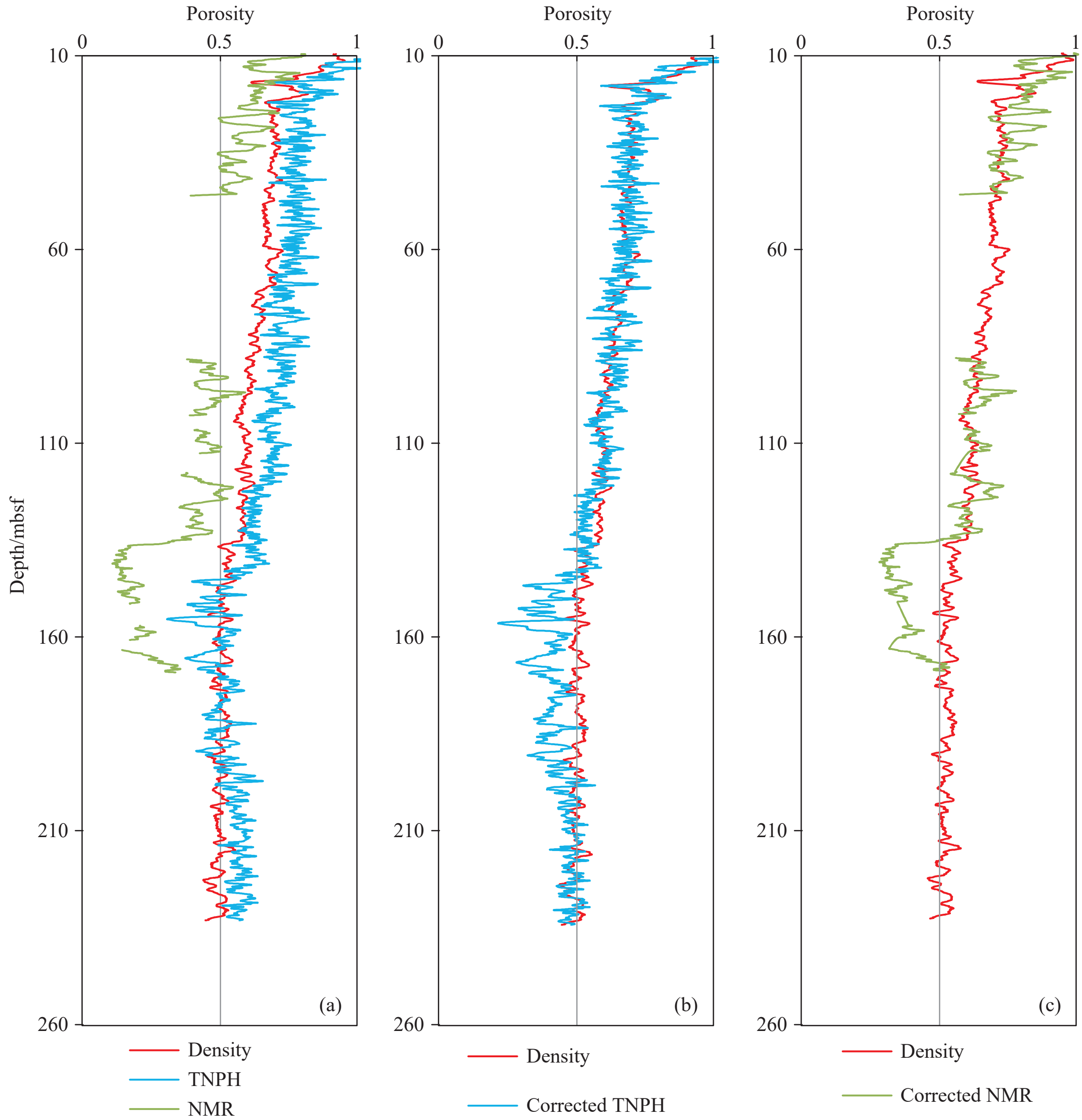

Fig. 4. Relationship of various porosities *vs.* depth at Site W19. a–comparison of neutron and NMR porosities with density porosity; b–corrected neutron porosity; c–corrected NMR porosity.

between the corrected NMR porosity and density porosity at a depth of 135–166 mbsf.

5. Gas hydrate saturations

Extensive literature on assessing gas hydrate saturations based on borehole LWD data has been reported (Lee MW et al., 1996; Tinivella and Carcione, 2001; Sun Y et al., 2011; Kang DJ et al., 2020). Among these data, the resistivity, velocity, and NMR logs are the most commonly applied in estimating gas hydrate concentration. Owing to the weak sonic Slowness-Time coherence in the target zone (Fig. 1), it is difficult to obtain reliable compressional slowness below the depth of 138 mbsf. Therefore, the gas hydrate concentration from the P-velocity is not introduced in this study. Instead, the gas hydrate saturation estimates of Site W19 based on the resistivity log and the limited NMR log are discussed as follows.

5.1. Estimates from resistivity

As previously discussed, the presence of gas hydrate will increase the values of formation resistivity, which indicates that the resistivity data can be used to calculate gas hydrate saturation. Archie's law can be used to obtain gas hydrate saturations (Archie GE, 1942). However, Archie's law is not accurate for shaly sands, where clay minerals are present in the formation matrices, as clay minerals have high conductivities that have significant effects on electrical resistivity (Lee MW and Collet TS, 2006). The ECS-derived mineral components indicate that the clay content is high at Site W19, with an average of 27.2% (Fig. 2). Therefore, the Simandoux model was used to account for the effects of clay (Simandoux P, 1963) in this study, and it can be formulated as:

$$\frac{1}{R_t} = \frac{\varphi_{d-ecs}{}^m}{aR_w} S_w{}^n + \frac{V_{sh}}{R_{sh}} S_w \tag{3}$$

$$S_h = 1 - S_w \tag{4}$$

where S_w and S_h are the water saturation and gas hydrate saturation, respectively, R_t represents the formation resistivity, R_w is the resistivity of connate water, V_{sh} is the volume fraction of clay derived from the ECS log, R_{sh} is the clay resistivity and is assumed to be 5 $\Omega \cdot m$, and a and m are Archie constants. The parameter n is the saturation exponent, which varies between 1.715 and 2.1661, depending on the lithology of reservoirs, and n = 1.9386 proposed by Pearson CF et al. (1983) for submarine sediments was used in this study.

The connate water resistivity (R_w) can be calculated using Arp's formula (Arp JJ, 1953) on the premise that the salinity and temperature of the formation water are known. Arp's formula is $R_{w2} = R_{w1}(T_1+7)/(T_2+7)$, where R_{w1} and R_{w2} are water resistivities at Fahrenheit temperatures at T_1 and T_2. According to the recovered core water samples at Site W19, the salinity and temperature gradient of the formation is 32–34 ppt and 5.6 °C/100 m, respectively.

The resistivity of fully saturated sediments (R_o) is proportional to the water resistivity (R_w) in the pore fluid, which can be expressed using the following equation:

$$R_O/R_w = a\phi^{-m} \tag{5}$$

R_O/R_w is defined as the formation factor (FF), and $FF = R_o/R_w$. Archie parameters a and m are calculated from a Pickett plot (Pickett GR, 1966), which is a cross-plot of FF and porosity of water-saturated sediments containing no gas hydrates and fitted with a power function. Fig. 5 shows the relation between FF and density porosity of the water-saturated interval from seafloor to 135 mbsf, which shows a very close correlation with regression coefficient (R^2 = 0.85). The Archie parameters a =1.12 and m=2.22.

It should be noted that both the density porosity and neutron porosity are not accurate between 162 mbsf and 190 mbsf due to the presence of the free gas in the pore space at Site W19. As is known, the free gas in the formation results in an increase in the density porosity and a decrease in the neutron porosity. Therefore, the formation porosity of the gas zone was corrected using the formula $\varphi = \sqrt{(\varphi_{d-ecs}{}^2 + \varphi_{corN}{}^2)/2}$, where φ_{corN} is the corrected neutron porosity.

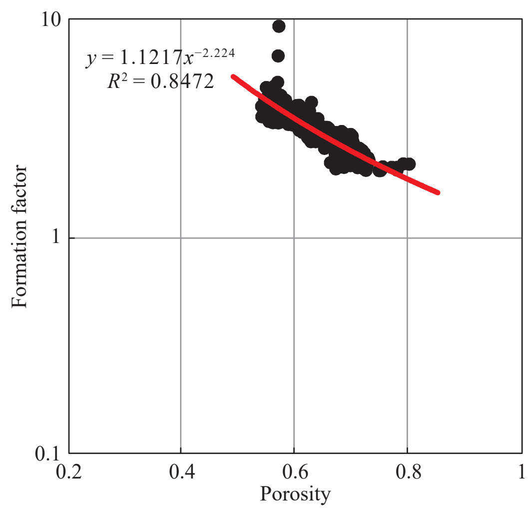

Fig. 5. Relationship between density porosity and formation factor. The data points are from fully water-saturated sediments from seafloor to 135 mbsf. The red line is the best linear fit providing Archie's parameters a and m.

Fig. 6 shows that the calculated R_o with a = 1.12 and m = 2.22 agreed well with the measured formation resistivity for most intervals, and the discrepancy is a result of the presence of gas hydrate and free gas in the formation.

Fig. 7a shows the calculated gas hydrate saturation from equation (3) based on the determined parameters (a = 1.12, m = 2.22, and n = 1.9386). Salinity in the pore fluid can be used to determine gas hydrate saturation as the decomposition of gas hydrate leads to pore-fluid freshening (Kvenvolden KA and Barnard LA, 1983; Kvenvolden KA and Kastner M, 1990; Paull CK et al., 1996). According to Fig. 7a, the calculated gas hydrate saturation from resistivity agreed well with the saturation estimated from the pore-water chemistry. For the gas hydrate zone at a depth of 135–162 mbsf, the average gas hydrate saturation was 39.2%, with a maximum of 63.4% in the pore space in the upper gas hydrate zone. Two gas zones at the interval from 162 mbsf to 166 mbsf and from 172 mbsf to 190 mbsf were observed at Site W19. The average gas saturations in these two zones were 14.8 % and 5%, respectively.

5.2. Estimates from NMR

The NMR log measures the hydrogen in the formation. Although gas hydrate contains abundant hydrogen in both its water and methane fractions, such hydrogen is invisible since the proVISION tool is not sensitive to hydrogen in solids (Kleinberg RL et al., 2003; Bauer K et al., 2015). Therefore, in the case that gas hydrate is present in the formation, the NMR porosity is reduced. The NMR porosity reflects the total pore space occupied by bound water, capillary water, and free

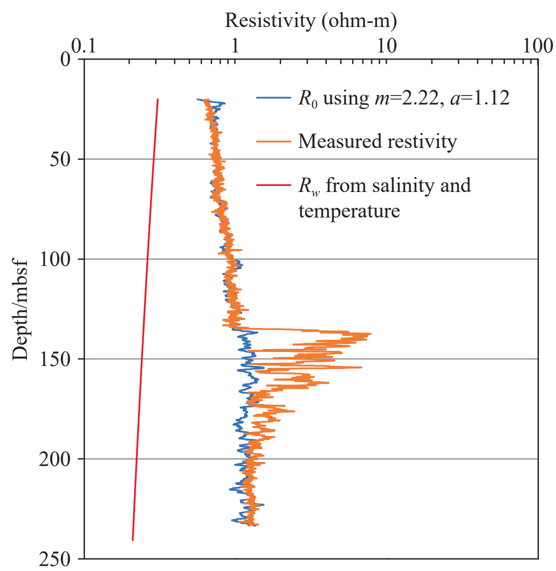

Fig. 6. Plot showing measured electrical resistivity (orange line), the pore-water resistivity (red line), and the background resistivity trend (blue line).

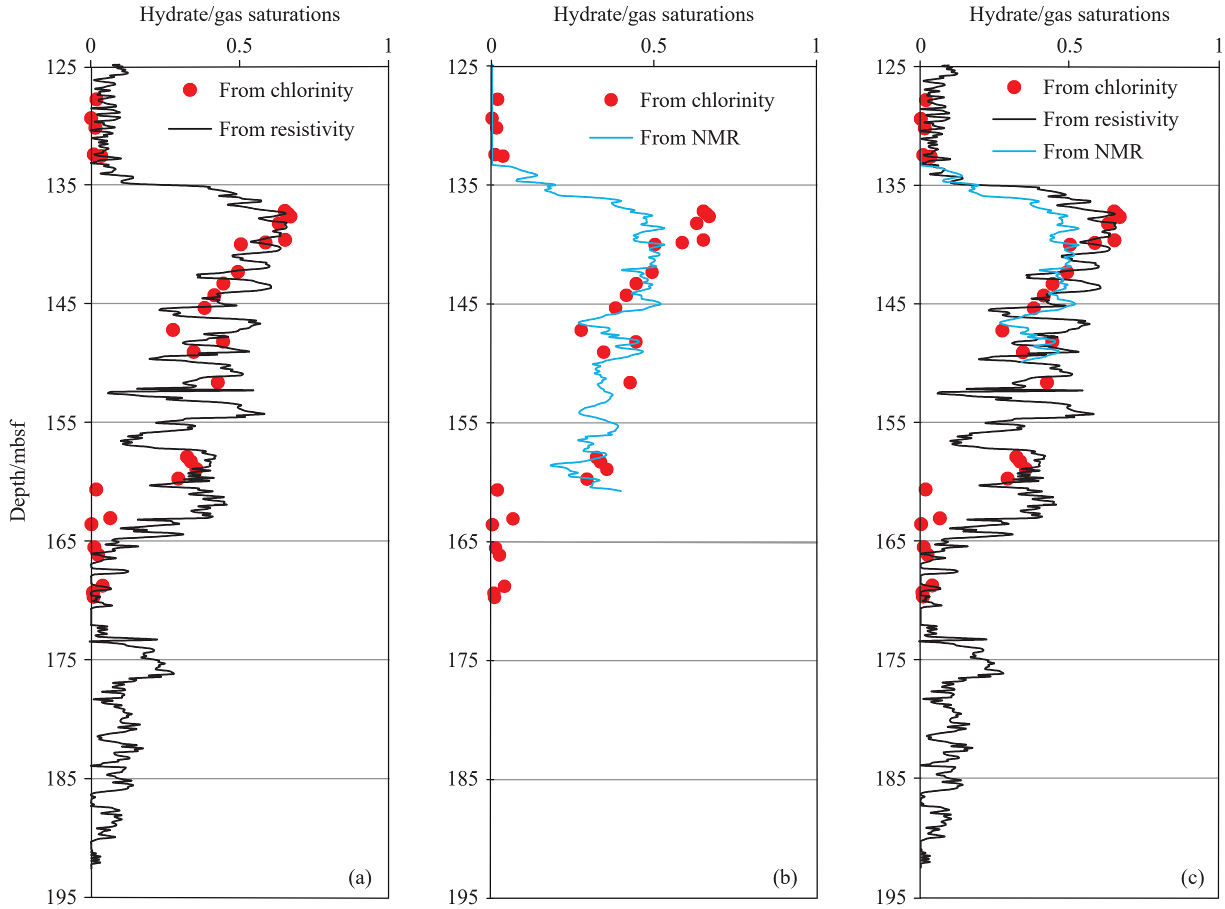

Fig. 7. Gas hydrate/gas saturations calculated from the resistivity (a) and NMR (b) logs and their comparison (c).

water. Ideally, NMR porosity equals the density porosity in water-bearing sediments, and the gas hydrate saturation can be given by the differences between the NMR and density porosities using the following equation:

$$S_h = (\varphi_{d-ecs} - \varphi_{corNMR})/\varphi_{d-ecs} \tag{6}$$

where S_h represents the gas hydrate saturation and φ_{corNMR} is the corrected NMR porosity by increasing by a factor of 0.16.

The gas hydrate saturation estimated from NMR is shown in Fig. 7b. It can be found that the estimated gas hydrate saturation roughly agreed with the saturation derived from pore water chemistry for most of the gas hydrate zone, but there were large differences in the upper part of the gas hydrate interval with a depth of 135–138 mbsf. The maximum gas hydrate concentration derived from pore water freshening was 71% (average: 65%) of pore volume in the range of about 135 –138 mbsf, while that derived from NMR was 50% (average: 46%), which was about 20% lower than that derived from pore water chemistry. The difference may mainly result from the inaccurate porosity extracted from the sparse NMR signal in the gas hydrate zone (Fig. 1).

6. Discussion

In this study, the bottom depth of the gas hydrate zone at Site W19 was determined at 162 mbsf. However, the density and neutron porosity logs were also inversely crossed above this depth. Additionally, the sonic Slowness-Time coherence became weak within the gas hydrate interval between 144.6 and 157 mbsf. All these indicate that free gas exactly occurs in the gas hydrate zone. The gas might originate from the decomposition of gas hydrates in the drilling process. Another possibility is that it is the free gas originally coexisting with the gas hydrates in the formation, which is also visible in the other gas hydrate reservoirs in the Shenhu area (Qian J et al., 2018; Li J et al., 2019; Qin XW et al., 2020). Even a small amount of free gas can cause the notable decrease in the neutron porosity due to the gas excavation effect. Therefore, if the free gas originally coexisted with the gas hydrates in the formation, it can be inferred free gas saturation is low since no clear decrease in density values was observed at this interval. In addition, the density and neutron porosity logs were inversely crossed, with the most distinct discrepancies occurring at the intervals of 144.8–146 mbsf, 149.1–149.8 mbsf, 151.1 –153.4 mbsf, and 154.5 –156.8 mbsf. The resistivity values were relatively low at these intervals (Fig. 8), which supports the interpretation of the low free gas saturation. The accurate saturation of gas hydrates and free gas in coexisting reservoirs will be further studied in the future.

The basis of logging interpretation and evaluation is to determine the mineral composition of the formation. Before detecting the minerals using XRD analysis, Site W19 was chosen as an ideal candidate site for gas hydrate production

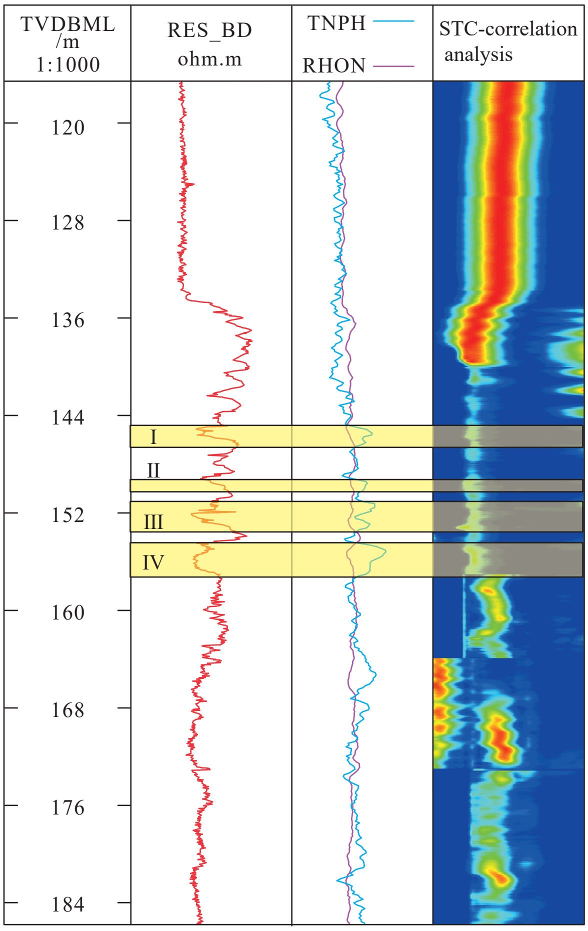

Fig. 8. Inverse intersection of density and neutron porosity logs of the gas hydrate zone.

testing due to its extremely high gas hydrate saturation (up to a maximum of about 66.9% as derived from the pore water freshening) and the low gamma response of the interval between 119 mbsf and 146 mbsf, which is believed to be caused by sands. In general, gas hydrate-rich sandy reservoirs are always considered to be the most potential targets for gas production (Dallimore SR and Collet TS, 2005; Anderson B et al., 2010). However, in this study, the increase in carbonate content induced by foraminifera contributed to the response of low gamma values, and the processing results of the ECS logging data also indicated the increase in carbonate content at the low gamma interval. Therefore, the unconventional ECS logging can be used to accurately measure the mineral composition of formation in the case of no retrieved core.

As is known, the porosity and saturation serve as two important parameters in reservoir assessment, and accurate porosity is the key to the assessment of gas hydrate saturation. Based on the ECS logging analysis of Site W19, more accurate density porosity was calculated using the matrix density calculated from ECS data, and it agreed well with the core porosities. Therefore, the density porosity can be used as the reference porosity, which allows the accuracy of the neutron and NMR porosities to be improved. Comparison between density, neutron, and NMR-derived porosities above the gas hydrate zone (Fig. 4a) reveals that the neutron porosity was generally higher but the NMR porosity was lower than the density porosity. According to the core and ECS log analyses, clay minerals are also the dominant minerals in the entire hole, and the presence of crystal water in the clay minerals is the primary cause for the elevation of the observed neutron readings. The neutron porosity was approximately 10% higher than the core data at the A1-SC well on Daini-Atsumi knoll (Suzuki K et al., 2015). The sediments in the Shenhu area are mainly composed of silty clay with abundant small pores in terms of lithology (Li JF et al., 2018; Li J et al., 2019; Kang DJ et al., 2019). Therefore, the large echo interval of the Schlumberger proVISION tool likely contributed to the loss of some small pores filled with clay-bound water, resulting in a lower NMR porosity in the zone without hydrates. Therefore, the neutron and NMR porosities were corrected by reducing by a factor of 0.09 and increasing by a factor of 0.16, respectively, and the corrected neutron and NMR porosities matched well with the density porosity above the gas hydrate zone (Figs. 4b, 4c).

After determining the formation porosity of Site W19, the authors estimated the gas hydrate saturation from the resistivity and NMR-density logs, expecting that the gas hydrate saturation calculated from the NMR-density logs can match well with that derived from the pore water freshening data because the gas hydrate concentration calculated from NMR-density logs is independent of models or parameters. As shown in Fig. 8b, the gas hydrate saturation estimated from the NMR agreed well with the core data for most parts of the gas hydrate zone. However, the average gas hydrate saturation estimated from the NMR log was approximately 20% lower than that derived from the pore water freshening data at the interval between 137.2 mbsf and 139.6 mbsf at the top of the gas hydrate zone. This is believed to be caused by the inaccurate NMR porosity resulting from the measurement failure of the ProVISION tool. Therefore, the accuracy of the gas hydrate saturation derived from the NMR and density logs mainly depends on the properties of NMR and density logs. In the case that clay minerals are present in the formation matrix, the resistivity affected by their high conductivities should be corrected using the models such as the Waxman-Smits mode for shaly sands (Waxman MH and Smits LJM, 1968) or the dual-water model proposed by Clavier C et al. (1984). In this study, the Simandoux model was used to assess the effects of the clay in order to derive accurate gas hydrate saturation of Site W19. As demonstrated in Fig. 7a, the gas hydrate saturation calculated using the Simandoux model agreed quite well with the core data of the gas hydrate zone. Fig. 7c shows the comparison of gas hydrate saturations calculated from the resistivity and NMR logs. According to this figure, the gas hydrate saturations were similar at a depth of 132–150 mbsf at Site W19. However, the gas hydrate saturations estimated from resistivity and NMR logs showed distinct differences in their value ranges, which were 0%–65.6% and 0%–53%, respectively. The possible reason is the proVISION tool did not work well in this well and resulted in accurate porosity. In addition, it should be noted that the resistivity of the gas hydrate reservoir at Site W19 has alternating high and low values. Therefore, it is more suitable for these types of strong saturation heterogeneity due to its higher vertical resolution (5.08–7.62 cm) than that of the NMR log (50.8 cm).

7. Conclusions

To characterize the gas hydrate reservoirs at Well W19 (which might be an ideal candidate site for potential gas hydrate production testing in the future), extensive geophysical logging data were used to obtain accurate mineral components, accurate porosity, and reasonable gas hydrate saturations. The following conclusions can be drawn.

(i) The gas hydrate-saturated and free gas intervals have been identified. The gas hydrate zone has a thickness of about 27 m and a depth interval of about 135–162 mbsf. Meanwhile, the free gas zone has a thickness of 28 m and a depth interval of 162–190 mbsf. The low gamma ray zone recorded by the LWD is caused by high carbonate content instead of sandy components according to the core analysis. The mineral composition calculated from the ECS logging data agrees well with the core data, and the mineral components mainly include quartz, carbonate, and clay, the average content of which is 44.3%, 20.6%, and 33.7%, respectively.

(ii) The average matrix density calculated using ECS-derived mineral components is 2.72 g/cm^3 and the determined density porosity within the gas hydrate-bearing interval varies in the range of about 45%–57%, with an average of 51.5%. The neutron and the NMR porosities must be corrected by reducing by a factor of 0.09 and increasing by a factor of 0.16, respectively to make them agree well with the density porosity.

(iii) The gas hydrate saturation has been estimated from the resistivity and NMR logs. The Simandoux model was used to account for the effects of clay in order to accurately estimate gas hydrate saturation. Compared to the values obtained from the NMR logs, the S_h values of the upper part of the gas hydrate zone estimated using the Simandoux model agree much better with the saturations derived from the salinity data. The possible reason is that the NMR porosity is not accurate due to the very sparse NMR signals. In addition, the vertical resolution of the NMR logs is lower than that of the resistivity logs. Therefore, resistivity is more suitable for these types of alternating high and low saturations. The S_h values obtained using the Simandoux model vary in the range of 0% –65.6%, with an average saturation of 42.7%. Meanwhile, the highest gas hydrate saturation occurs in the upper 3 m of the hydrate-bearing zone. The average saturation of the underlying free gas is 10% as derived from the resistivity log using the Simandoux model.

CRediT authorship contribution statement

Dong-ju Kang, Ying-feng Xie, Jing-an Lu and Jin-qiang Liang conceived of the presented idea. Tong Wang, Hong-fei Lai and Yun-xin Fang contributed to the log and core data preparation. All authors discussed the results and contributed to the final manuscript.

Declaration of competing interest

The authors declare no conflicts of interest.

Acknowledgment

This research was jointly supported by the Key Area Research and Development Program of Guangdong Province (2020B1111030003), the Key Special Project for Introduced Talents Team of Southern Marine Science and Engineering Guangdong Laboratory (Guangzhou) (GML2019ZD0102) and the Project of China Geological Survey (DD20221700). The authors are grateful to those contributing to the success of the GMGS3 Expedition in the Shenhu area.

References

Anderson B, Hancock S, Wilson S, Enger C, Collett T, Boswell R, Hunter R. 2010. Formation pressure testing at the Mount Elbert Gas Hydrate Stratigraphic Test Well, Alaska North Slope: Operational summary, history matching, and interpretations. Marine and Petroleum Geology, 28, 478–492. doi: 10.1016/j.marpetgeo.2010.02.012.

Archie GE. 1942. The electrical resistivity log as an aid in determining some reservoir characteristics. Journal of Petroleum Technology, 1, 55–62.

Arp JJ. 1953. The effect of temperature on the density and electrical resistivity of sodium chloride solutions. Petroleum Transaction, American Institute of Mining, Metallurgical, and Petroleum Engineers, 198(10), 17–20. doi: 10.2118/953327-G.

Bauer K, Kulenkampff J, Henninges J, Spangenberg E. 2015. Lithological control on gas hydrate saturation as revealed by signal classification of NMR logging data. Journal of Geophysical Research Solid Earth, 120(9), 6001–6017. doi: 10.1002/2015JB012150.

Clavier C, Coates G, Dumanoir J. 1984. Theoretical and Experimental Bases for the Dual-Water Model for Interpretation of Shaly Sands. Society of Petroleum Engineers, 24(02), 153–168. doi: 10.2118/6859-PA.

Collett TS, Ladd J. 2000. Detection of gas hydrate with downhole logs and assessment of gas hydrate concentrations (saturations) and gas volumes on the Blake Ridge with electrical resistivity log data. Proceedings of the Ocean Drilling Program:Scientific Results, 164, 179–191. doi: 10.2973/odp.proc.sr.164.219.2000.

Cui Y, Lu C, Wu M, Peng Y, Yao Y, Luo W. Review of exploration and production technology of natural gas hydrate. Advances in Geo-Energy Research, 2018, 2(1): 53 –62. https://doi.org/10.26804/ager.2018.01.05.

Dallimore SR, Collet TS. 2005. Scientific Results from the Mallik 2002 Gas Hydrate Production Research Well Program, Mackenzie Delta, Northwest Territories, Canada. Bulletin of the Geological Survey of Canada. doi: 10.4095/220702.

Fujii T, Suzuki K., Takayama, T., Tamaki, M., Komatsu, Y., Konno, Y., Yoneda J., Yamamoto K., Nagao, j. 2015. Geological setting and characterization of a methane hydrate reservoir distributed at the first offshore production test site on the daini-atsumi knoll in the eastern Nankai Trough, Japan. Marine & Petroleum Geology, 66, 310–322. doi: 10.1016/j.marpetgeo.2015.02.037.

Kang DJ, Liang JQ, Kuang ZG, Lu JA, Guo YQ, Liang JJ, Cai HM, Qu CW. 2018. Application of elemental capture spectroscopy logging in hydrate reservoir evaluation in the Shenhu sea area. Natural Gas Industry, 38(12), 60–66. doi: 10.3787/j.issn.1000-0976.2018.12.006.

Kang DJ, Lu JA, Qu CW, Wang JL, Xie YF, Lai HF, Wang XJ, Liang JQ. 2020. Characteristics of gas hydrate reservoir determined from logging-while-drilling resistivity image data in the Shenhu area.

Journal of Environmental Geotechnics, 1–7. doi: 10.1680/jenge.19.00016.

Kenyon WE. 1992. Nuclear magnetic resonance as a petrophysical measurement. International Journal of Radiation Applications & Instrumentation. part E. nuclear Geophysics, 6(2), 153–171. doi: 10.1016/0892-6875(92)90067-J.

Kleinberg RL, Flaum C, Griffin DD, Brewer PG, Malby GE, Peltzer ET, Yesinowski JP. 2003. Deep Sea NMR: Methane hydrate growth habit in porous media and its relation to hydraulic permeability, deposit accumulation, and submarine slope stability. Journal of Geophysical Research, 108(B10), 2508. doi: 10.1029/2003JB002389,2003.

Kleinberg RL. 1999. Nuclear magnetic resonance. Experimental Methods in the Physical Sciences, 35, 337–385. doi: 10.1016/S0076-695X(08)60420-2.

Kvenvolden KA, Barnard LA. 1983. Gas hydrate of the Blake Outer Ridge, site 533, Deep Sea Drilling Project leg 76, in Orlofsky S(Ed.). Proceedings of the Ocean Drilling Program, Initial Reports, 76, 353–365

Kvenvolden KA, Kastner M. 1990. Gas hydrate of the Peruvian outer continental margin, in Stewart SK (Ed.). Proceedings of the Ocean Drilling Program, Scientific Results, 112, 517–526. doi: 10.2973/odp.proc.sr.112.147.1990.

Latour LL, Kleinberg RL, Mitra PP, Sotak CH. 1995. Pore-size distributions and tortuosity in heterogeneous porous media. Journal of Magnetic Resonance, 112(1), 83–91. doi: 10.1006/jmra.1995.1012.

Lee MW, Collett TS. 2006. A method of shaly sand correction for estimating gas hydrate saturations using downhole electrical resistivity log data. U. S. Geological Survey Scientific Investigations Report 2006-5121, 10 p

Lee MW, Collett TS. 2009. Gas hydrate saturations estimated from fractured reservoir at site NGHP-01-10, Krishna-Godavari basin, India. Journal of Geophysical Research: Solid Earth, 114, B07102. doi: 10.1029/2008JB006237.

Lee MW, Collett TS. 2011. In-situ gas hydrate saturation estimated from various well logs at the Mount Elbert Gas Hydrate Stratigraphic Test Well, Alaska North Slope. Journal of Marine and Petroleum Geology, 28(2), 439–449. doi: 10.1016/j.marpetgeo.2010.02.007.

Lee MW, Collett TS. 2012. Pore- and fracture-filling gas hydrate reservoirs in the Gulf of Mexico gas hydrate joint industry project leg II green canyon 955 H well. Marine and Petroleum Geology, 34, 62–71. doi: 10.1016/j.marpetgeo.2011.08.002.

Lee MW, Hutchinson DR, Collett TS, Dillon WP. 1996. Seismic velocities for hydrate-bearing sediments using weighted equation. Journal of Geophysical Research, 101(B9), 20347–20358. doi: 10.1029/96JB01886.

Li J, Lu JA, Kang DJ, Ning FL, Lu HF, Kuang ZG, Wang DD, Liu CL, Hu GW, Wang JS, Liang JQ. 2019. Lithological characteristics and hydrocarbon gas sources of gas hydrate-bearing sediments in the Shenhu area, south China sea: implications from the sc-w01b and sc-w02b sites. Marine Geology, 408, 36–47. doi: 10.1016/j.margeo.2018.10.013.

Li JF, Ye JL, Qin XW, Qiu HJ, Wu NY, Lu HL, Xie WW, Lu JA, Peng F, Xu ZQ, Lu C, Kuang ZG, Wei JG, Liang QY, Lu HF, Kou BB. 2018. The first offshore natural gas hydrate production test in South China Sea. China Geology, 1, 5–16. doi: 10.31035/cg2018003.

Li, Y., Liu, L., Jin, Y., Wu, N. Characterization and development of natural gas hydrate in marine clayey-silt reservoirs: A review and discussion. Advances in Geo-Energy Research, 2021, 5(1): 75–86. https://doi.org/10.46690/ager.2021.01.08.

Paull CK, Matsumoto R, Wallace PJ. 1996. In: Proceedings of ODP Initial Reports, 164: College Station, Texas, 459 pp

Pearson CF, Halleck PM, Mcguire PL, Hermes R, Mathews M. 1983. Natural gas hydrate deposits: a review of in situ properties. The Journal of Physical Chemistry, 97, 4180–4185. doi: 10.1021/j100244a041.

Pickett GR. 1966. A review of current techniques for determination of water saturation from logs. Journal of Petroleum Technology, 11, 1425–1433.

Qian J, Wang XJ, Collett TS, Guo YQ, Kang DJ, Jin JP. 2018. Downhole log evidence for the coexistence of structure II gas hydrate and free gas below the bottom simulating reflector in the South China Sea. Marine and Petroleum Geology 98, 662–674. doi: 10.1016/j.marpetgeo.2018.09.024.

Qin XW, Lu JA, Lu HL, Qiu HJ, Liang JQ, Kang DJ, Zhan LS, Lu HF, Kuang ZG. 2020. Coexistence of natural gas hydrate, free gas and water in the gas hydrate system in the Shenhu Area, South China Sea. China Geology, 2(2020), 210–220. doi: 10.31035/cg2020038.

Simandoux P. 1963. Dielectric measurements in porous media and application to shaly formations.

Sun Y, Goldberg D, Collett T, Hunter R. 2011. High-resolution well-log derived dielectric properties of gas-hydrate-bearing sediments, Mount Elbert Gas Hydrate Stratigraphic Test Well, Alaska North Slope. Journal of Marine and Petroleum Geology 28 (2), 450–459. doi: 10.1016/j.marpetgeo.2010.03.001.

Suzuki K, Takayama T, Fujii T. 2015. Density structure report from logging-while-drilling data and core data at the first offshore gas production test site on Daini-Atsumi knoll around eastern Nankai Trough. Marine and Petroleum Geology, 388–395. doi: 10.1016/j.marpetgeo.2015.02.026.

Tinivella, Carcione. 2001. Estimation of gas-hydrate concentration and free-gas saturation from log and seismic data. Geophysics, 20(2), 1568. doi: 10.1190/1.1438914.

Shankar U, Riedel M. 2014. Assessment of Gas Hydrate Saturation in Marine Sediments from Resistivity and Compressional-wave Velocity Log Measurements in the Mahanadi Basin, India. Marine and Petroleum Geology, 58, 265–277. doi: 10.1016/j.marpetgeo.2013.10.007.

Waxman MH, Smits LJM. 1968. Electrical conductivities in oil-bearing shaly sand. Society of Petroleum Engineers Journal, 8, 107–122. doi: 10.2118/1863-A.

Wei JG, Fang YX, Lu HL, Lu HF, Lu JA, Liang JQ, Yang SX. 2018. Distribution and characteristics of natural gas hydrates in the Shenhu Sea Area, South China Sea. Marine and Petroleum Geology, 98, 622–628. doi: 10.1016/j.marpetgeo.2018.07.028.

Yamamoto K, Terao, Y, Fujii T, Ikawa, T, Seki M, Matsuzawa M, Kanno T. 2014. Operational overview of the first offshore production test of methane hydrates in the Eastern Nankai Trough. In: Proceedings of 2014 Offshore Technology Conference, Houston, Texas, U. S. A. , OTC 25243

Ye JL, Qin XW, Xie WW, Lu HL, Ma BJ, Qiu HJ, Liang JQ, Lu JA, Kuang, ZG, Lu C, Liang QY, Wei SP, Yu YJ, Liu CS, Li B, Shen KX, Shi HX, Lu QP, Li J, Kou BB, Song G, Li B, Zhang HE, Lu HF, Ma C, Dong YF, Bian H. 2020. The second natural gas hydrate production test in the South China Sea. China Geology, 3(2), 197–209. doi: 10.31035/cg2020043.

Zhang GX, Yang SX, Zhang M, Liang JQ, Lu JA, Holland M, Schultheiss P. 2014. GMGS2 expedition investigates rich and complex gas hydrate environment in the South China Sea. Fire Ice 14, 1–5.

Zhang HQ, Yang SX, Wu NY, Xu X, Melanie H, Peter S, Kelly R, Heather B, Gary H, GMGS1-1 Science Team. 2007. Successful and surprising results for China's first gas hydrate drilling expedition. Fire in the ice, 7, 6–9.

Zhong J, Hou XL, Zhu WL, Shi GH, Gao X, Li F. 2019. Design of Control Timing for 0.3 ms Short Echo Interval of NMR Logging Tool. Well Logging Technology, 43(4), 365–368.